Feature Density Based Terrain Hazard Detection for Planetary Landing

AI GAO
SHIBO ZHOU
Beijing Institute of Technology, Beijing, China

To ensure successful future planetary landing mission, the lander must be capable of detecting and assessing terrain hazard in the nominal landing zone. This paper presents an innovative method of planetary terrain hazard detection. The concept of feature density is introduced into the process of terrain hazard detection. Moreover, the statistical information of the terrain feature density is utilized to represent the terrain hazard level. Opposed to other methods of hazard detection, the research in this paper focuses on how to build a unified terrain representation by the terrain features rather than detecting the specific one or several types of hazard obstacles in traditional sense. Computer simulations demonstrates that the method presented in this paper is able to conduct multitype of complex terrain hazard detecting by the terrain feature detected in the visual image obtained from onboard camera during the landing phase.

Manuscript received September 29, 2016; revised November 18, 2017; released for publication January 31, 2018. Date of publication March 22, 2018; date of current version October 10, 2018.

DOI. No. 10.1109/TAES.2018.2818578

Refereeing of this contribution was handled by H. Kwon.

This work was supported in part by the Young Elite Scientist Sponsorship Program by CAST (YESS) under Grant 2016QNRC001, in part by the National Basic Research Program of China (973 Program) under Grant 2012CB720000, in part by the National Natural Science Foundation of China under Grant 61304226, and in part by the Science and Technology Innovation Team of Beijing Institute of Technology.

Authors' address: A. Gao and S. Zhou are with the School of Aerospace Engineering, Beijing Institute of Technology, Beijing 100081, China, E-mail: (gaoai@bit.edu.cn; zhoushibo@bit.edu.cn). *(Corresponding author: Ai Gao.)*

I. INTRODUCTION

Autonomous safe landing is an important capability required to ensure mission success for future planetary landing missions. Previous planetary landing missions mostly selected large, safe but scientifically less interesting sites for the landers that had no closed-loop sensory feedback on hazards in the potential landing area [1]. Future landing missions will target scientifically interesting features that lie in areas, which are most likely near craters, ridges, fissures, and other relevant geological formations, far more hazardous than those attempted by previous landers [2]. These sites are difficult to be observed at high resolution before landing exploration and even they are not known *a priori* [3]. To land safely, future landers must be capable of detecting and assessing terrain hazard [4].

Several studies of terrain hazard detection have been carried out in the past, the digital terrain elevation map (DEM) acquired by active sensors (such as lidar) based hazard detection method, represented by the ALHAT project, is a hot topic in the field of hazard detection [5]. These methods can directly measure the depth of sensed terrain and determine slop and roughness by local plane fitting, suitable for a variety of hazards detection, but there are still problems such as measuring outliers and the terrain reference deviation [6]. Lidars in the current state-of-the-art are costly, heavy, with high power consumption and low resolution, which cannot become the choice for low-cost/small-size missions [7]. On the contrary, passive image acquired by cameras-based hazard detection methods need lower weight, lower cost, lower power consumption, wider field of view, and higher resolution. These advantages make passive image-based methods suitable for low-cost missions [8]–[10]. Hazardous terrains can be classified in four types: rocks, craters, slopes, and discontinuities. In the studies of rocks detection, Matthies *et al.* [11] provided a local terrain plane fitting method using stereo vision reconstruct landing terrain 3-D model to fulfill rock detection. In addition, Matthies *et al.* [11], Woicke and Mooij [12], Bajracharya [13], and Huertas *et al.* [14] made contributions to hazard detection and problems under poor light environment conditions through the use of illumination and shadow analysis. As the shapes of the rocks are not easy to describe, for the complex shapes and locations of the rocks detection is still a problem to be solved. In the studies of craters detection, Leroy *et al.* [15] studied asteroid's crater detection and provide a shadow edge curve fitting based crater detection method. Barata *et al.* [16] investigated template matching and principal component analysis theory and improved the accuracy of detections. Martins *et al.* [17] also studied different scale crater detection problem and presented a boosting approach method. The difficulties of craters detection methods are the detections of irregular craters and nonobvious craters [18]. In the studies of slopes and discontinuities, Cheng *et al.* [8] provided candidate landing areas in a single image by measuring standard deviation of the pixels' gray value from the image window. Then, using homography theory, they verified whether the slope level

in candidate areas satisfied mission's requirement. Johnson *et al.* [19] presented a hazard detection method based on image depth information, which is obtained by machine vision and camera motion information. Slopes terrain need the accurate measurements of the landing terrain, single image based methods still need to solve the problems of motion estimation accuracy and image matching accuracy. These studies make great contribution to the development of terrain hazard detection for planetary landing. For the complex multitypes terrain, the combination of these methods will not be suitable for the low-cost/small-size missions [20]–[23]. Hence, it is important to find a unified terrain hazard detection method, which satisfied the requirements of complex and scientific terrain landing safety.

This paper presents an innovative method of planetary terrain hazard detection. In particular, the research focuses on searching a unified representation of terrain hazard by terrain feature rather than detecting the specific one or several types of terrain hazard in traditional sense. First, the difficulties of multitypes terrain hazard detection are analyzed. Second, the concept of feature density is introduced into the process of terrain hazard detection and assessment, and the framework of feature density based terrain hazard detection and assessment method is given. Moreover, the calculation formula of terrain feature density is derived by Gaussian processes machine learning. Then, the terrain assessment criteria based on feature density is established. Finally, the method proposed in this paper is applied to different types of terrain hazard detection and assessment, which the simulation data comes from the visual image published by prior missions. Simulation results show that the method exhibits good performance in conducting multiple types of complex terrain hazard detecting and assessing.

II. IMAGE FEATURE POINT EXTRACTION METHOD

Under natural illumination, terrain hazards, such as rocks, craters, slopes, and discontinuities, form clearly shadows and textures in visual images. Feature points detection algorithms can extract the feature points of terrain hazards. These feature points can be described as the terrain features. Using different feature points extraction methods, the feature points' positions and total number can be different. Therefore, the image taken during landing trajectory should select the suitable feature point detection method. The common feature point detection methods include template-based detection methods (Harris, FAST, SUSAN), difference-based methods (LoG, Canny, Sobel), and scale-space-based methods (SIFT, SURF). Fig. 1 shows the image of the curiosity landing zone from the Mars orbiter. The distribution of the feature points extracted by different feature points methods are shown in Fig. 1. The run time and the number of feature points are shown in Table I. Scale-space-based methods (such as SIFT) have appropriate numbers but a relatively long run time. Harris operator and FAST operator, although running faster, have many noise points. SUSAN algorithm is less sensitive to noise, but the detection efficiency is low. Difference-based methods are generally computationally efficient, but still have bias points. Compared with scale-space-based methods, difference-based have satisfied the capability of expressing terrain features. Considering the onboard computing ability, the feature points extraction method should be within 100 ms. In this paper, we use "Sobel operator" as the feature point extraction method.

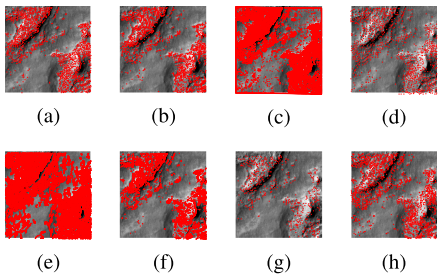

Fig. 1. Feature points extracted from different methods.

TABLE I
Run Time and Numbers of the Points

Algorithm	Run time	Numbers
Harris	27.502147ms	1683
FAST	1.707435ms	1994
SUSAN	2452.833351ms	39121
LoG	739.333704ms	1050
Canny	16.435117ms	32916
Sobel	2.396490ms	7362
SIFT	889.330204ms	2028
SURF	18.075869ms	513

III. FEATURE DENSITY BASED HAZARD DETECTION AND TERRAIN ASSESSMENT METHOD

A. Framework of Terrain Hazard Detection and Assessment

The feature points are extracted from the edges of the hazards. Therefore, the density of the features can directly reflect the distribution characteristic of the terrain hazards. Inspired by this finding, we introduce the concept of feature density into building a unified representation of terrain hazard, which is derived by Gaussian process machine learning. The terrain assessment criteria are established based on feature density. The framework of feature density based terrain hazard detection and assessment is given in the following and the diagram is given in Fig. 2 and Table II. Different from other terrain hazard detection and assessment methods, the method proposed in this paper only detects the terrain feature points and assesses the terrain hazard using the representation of feature density directly, which avoids the terrain hazard assessment suffering from the difficulties in the detection of complex terrain hazards mentioned above. It is worth noting that the terrain feature density plays an important role in this method, and how to derive the terrain feature density is the basis and the key of the whole method. Section III-B gives the calculation method of the terrain feature density.

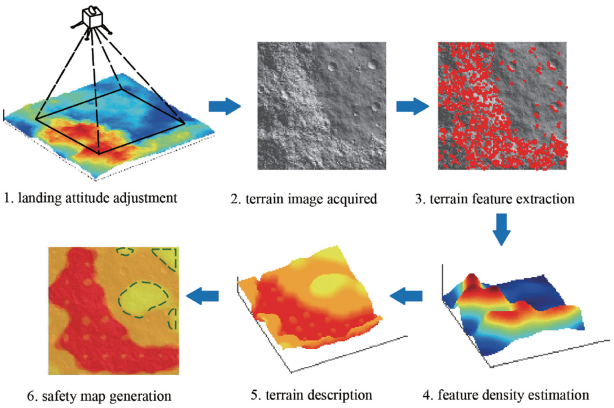

Fig. 2. Diagram of feature density based terrain hazard detection and assessment.

TABLE II
Framework of Feature Density Based Terrain Hazard Detection and Assessment

Step 1	Lander adjusts the attitude to have a good vision of the landing zone.
Step 2	The onboard camera captures the images of the landing zone.
Step 3	The landing images are conducted by filtering to reduce the image noise. And the feature points are extracted by the detection algorithm.
Step 4	The feature density, as a unified representation of terrain hazard, is calculated with the information of the terrain feature points.
Step 5	The feature density redescribes the terrain of the landing zone. And the terrain assessment criteria is established by synthesizing the statistical information of feature density.
Step 6	The safety map of the landing zone is generated by the assessment criteria based on feature density.

B. Calculation Method of Feature Density

1) *Spatial Point Density Estimation Method:* In the density-based hazard detection method, the estimation of the density is important. The distribution of feature points' locations is limited in the finite image plane, and the distribution of the feature points is independent. Hence, the distribution of the feature points can be regarded as the spatial point pattern, which means the distribution of the feature points' locations satisfies the definition of the spatial point process. The density of the feature points usually use the first-order effects of the measure, including quadrat analysis, kernel density estimation. The quadrat sampling method is using quadrats to sample the points uniformly or randomly, the quadrats could be square, circular, or even irregular. Then, the density function is obtained from the sampling results.

As shown in Fig. 3, the results of density estimation are greatly affected by the shape and size of the quadrats. In some circumstances, random sampling of the points cannot fully describe the points' density. The kernel density method regards each feature point as a kernel function, so the density function can be considered as the result of the superposition of the kernel function from each feature point. As shown in Fig. 4, the method is greatly affected by the radius of the kernel function, and the calculation of density estimation is connected to the number of feature points. The

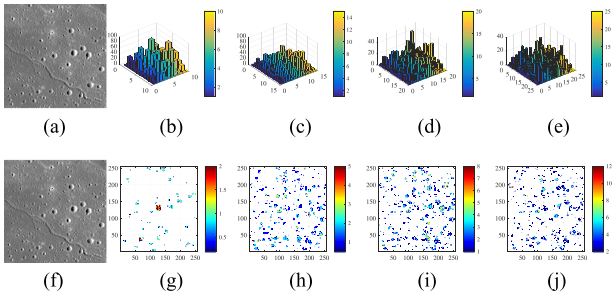

Fig. 3. Density calculated by quadrat analysis.

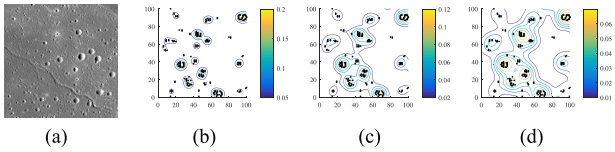

Fig. 4. Density calculated by the kernel function method.

density function of the spatial point process can indirectly describe the position distribution of the feature points on the plane. Since the spatial point process satisfies the two-dimensional Poisson process (spatial Poisson process), the Gaussian process machine learning method can be used to calculate the density function of the spatial Poisson process.

2) *Gaussian Processes Machine Learning Framework:* Gaussian process machine learning is a kind of the Bayesian statistical learning theory based machine learning method, which is suitable for dealing with nonlinear small-capacity sample problem. Bayesian inferences based Gaussian process machine learning method can effectively approximate the non-Gaussian process to the Gaussian process and obtain a relatively fast and accurate estimation result. This method was first proposed by Krige for the estimation of the distribution of gold in mines [24]. Thus far, the method has been applied to the field of aerospace research and includes prior work on the aircraft's airfoil design [25], aircraft's aerodynamic coefficient assessment [26], and for the assessment of the main belt that asteroids can reach [27].

In general, we define that the machine learning dataset Θ is

$$\Theta = (\tilde{u}, \tilde{v}) \tag{1}$$

where $\tilde{u}_k$ and $\tilde{v}_k$ construct the input matrix $\tilde{u} = [\,\tilde{u}_1 \cdots \tilde{u}_n\,]^T$ and output matrix $\tilde{v} = [\,\tilde{v}_1 \cdots \tilde{v}_n\,]^T$. In the framework of Bayesian inferences, the Gaussian process mainly achieves the description of latent function $f(\tilde{u})$[28]. Based on the definition of Bayes formula [29]

$$p(f|\Theta, \theta, \phi) = \frac{p(\tilde{v}|f, \phi)\, p(f|\tilde{u}, \theta)}{\int p(\tilde{v}|f, \phi)\, p(f|\tilde{u}, \theta)\, df} \tag{2}$$

where θ is the parameter of latent function f and ϕ is the parameter of observation model. $p(f|\tilde{u}, \theta)$ is the prior of latent function, $p(\tilde{v}|f, \phi)$ is the likelihood of latent function, and $p(f|\Theta, \theta, \phi)$ is the posterior of the latent function. The new input is marked as u^* and the latent function's output is marked as $\tilde{f} = f(\tilde{u})$ and $f^* = f(u^*)$. Based on Bayesian

inferences, the distribution of observation output v^* is [30]

$$p\left(v^*|\Theta, u^*, \theta, \phi\right) = \int p\left(v^*|f^*, \phi\right) p\left(f^*|\Theta, u^*, \theta, \phi\right) df^*. \quad (3)$$

If the observation model v is a Gaussian process, then the distribution of $p\left(v^*|f^*, \phi\right)$ is normal distribution. The observation outputs are the same as the latent function's outputs. The distribution of $p\left(f|\Theta, u, \theta, \phi\right)$ is also a normal distribution. So the distribution of $p\left(v^*|\Theta, u^*, \theta, \phi\right)$ can be expressed as

$$v^*|\Theta, u^*, \theta \sim N\left(C_{u^*\tilde{u}}C_{\tilde{u}\tilde{u}}^{-1}\tilde{v}, C_{u^*u^*} - C_{u^*\tilde{u}}C_{\tilde{u}\tilde{u}}^{-1}C_{\tilde{u}u^*}\right) \quad (4)$$

where $C_{\tilde{u}\tilde{u}} = Cov[f(\tilde{u}), f(\tilde{u})]$, $C_{\tilde{u}u^*} = Cov[f(\tilde{u}), f(u^*)]$, $C_{u^*\tilde{u}} = Cov[f(u^*), f(\tilde{u})]$, $C_{u^*u^*} = Cov[f(u^*), f(u^*)]$. $Cov[\bullet, \bullet]$ is the covariance matrix. The covariance matrix is made up by kernel functions in general. The mean value E and covariance Cov of the latent function can be expressed as

$$E_{f^*} = C_{u^*\tilde{u}}C_{\tilde{u}\tilde{u}}^{-1}\tilde{f} \quad (5)$$

$$Cov_{f^*} = C_{u^*u^*} - C_{u^*\tilde{u}}C_{\tilde{u}\tilde{u}}^{-1}C_{\tilde{u}u^*}. \quad (6)$$

For the non-Gaussian observation model, the distribution of $p\left(f|\Theta, \theta, \phi\right)$ cannot be expressed as normal distribution and the integral of (3) cannot be calculated simply [31]. Therefore, it is necessary to use Laplace approximation to calculate the posterior $p\left(f|\Theta, \theta, \phi\right)$, which means a second Taylor expansion

$$p\left(f|\Theta, \theta, \phi\right) \approx q\left(f|\Theta, \theta, \phi\right) = N\left(f|\hat{f}, \left(C_{\tilde{u}\tilde{u}}^{-1} + Q\right)^{-1}\right) \quad (7)$$

where $\hat{f} = \arg\max_{\tilde{f}}\left[p\left(\tilde{f}\middle|\tilde{u}, \tilde{v}\right)\right]$, $\arg\max$ means the finding the $\tilde{f}$ when $p\left(\tilde{f}\middle|\tilde{u}, \tilde{v}\right)$ got the maximum value. Q is the negative Hessian matrix of $\ln p\left(\tilde{v}|\tilde{f}\right)$:

$$Q = -\nabla\nabla \ln p\left(\tilde{v}|\tilde{f}\right). \quad (8)$$

When substituting $\hat{f}$ and Q into (5) and (6), we can obtain

$$E_{f^*} = C_{u^*\tilde{u}}C_{\tilde{u}\tilde{u}}^{-1}\hat{f} \quad (9)$$

$$Cov_{f^*} = C_{u^*u^*} - C_{u^*\tilde{u}}\left(C_{\tilde{u}\tilde{u}} + Q^{-1}\right)^{-1}C_{\tilde{u}u^*}. \quad (10)$$

These are the output mean E_{f^*} and covariance Cov_{f^*} of latent function f when the input is u^*.

3) *Gaussian-Processes-Based Density Estimation Method:* Landing image is a 2-D plane bounded by cameras' field of view (FOV) and feature points in this plane are isolated, which satisfied the definition of spatial inhomogeneous Poisson point processes [31]. The density of feature points in the image can be approximated by the intensity function $\lambda(u)$ of the point processes whose u is pixel's coordinate. Consider using log Gaussian processes to describe the intensity function $\lambda(u)$, the point processes become log Gaussian Cox processes whose intensity function could be expressed as (11), where $f(u)$ are Gaussian processes [32]. Hence, we can use Gaussian processes machine learning method modeling $f(u)$ and further modeling $\lambda(u)$ as follows:

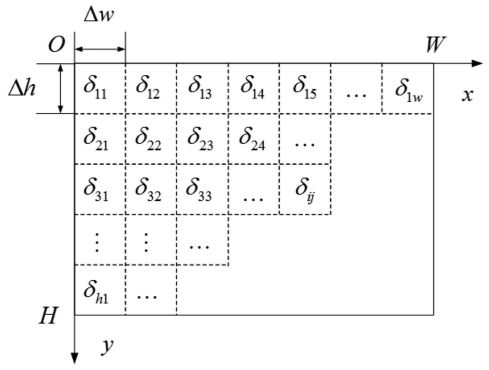

Fig. 5. Image coordinate definition and cells division.

$$\lambda(u) = \exp\{f(u)\} \quad (11)$$

where $f(u)$ are Gaussian processes, and we can use the machine learning method to describe these Gaussian processes. Furthermore, we can obtain the statistical characteristics of density $\lambda(u)$, which are also the characteristics of the feature points' density.

Define landing image's coordinate center at the top-left corner, the x axis has W pixels and y axis has H pixels, the directions of axes are shown in Fig. 5. The filtered and denoised image is segmented with n isolated grid cells δ_{ij}, as shown in Fig. 4, where $n = w \times h$. The cells are rectangles with same size of $\Delta w \times \Delta h$ and divide the image with w cells in x axis and h cells in y axis. δ_{ij} is a single cell at row i column j ($i = 1, 2, \ldots, h \quad j = 1, 2, \ldots, w$) and the number of feature points are γ_{ij} in δ_{ij}. The cells center's coordinate is $[\, p_{ij}^x \;\; p_{ij}^y \,]$, where $p_{ij}^x = (j - 0.5)\Delta w$ and $p_{ij}^y = (i - 0.5)\Delta h$.

The points number in δ_{ij} and the cell center's coordinate are the data source of machine learning, as shown in (2), where input training data $\tilde{u}_k$ are the normalized coordinates and output training data $\tilde{v}_k$ are γ_{ij}:

$$\begin{cases} \tilde{u}_k = \left[\, \frac{1}{W}p_{ij}^x \;\; \frac{1}{H}p_{ij}^y \,\right]^T \\ \tilde{v}_k = \gamma_{ij} \end{cases} \quad (k = 1, 2, \ldots n). \quad (12)$$

Based on (1), we cannot directly describe $\lambda(u)$ using Gaussian processes because the distribution of $p\left(\tilde{v}|f, \phi\right)$ is non-Gaussian. Moller *et al.* [32] assumed that the intensity of a discretize region can be locally constant, so the feature point distribution within the image grid can be approximated by a stationary Poisson processes:

$$p\left(\tilde{v}|\tilde{f}\right) \approx \prod_{k=1}^{n} \text{Poisson}\left(\tilde{v}_k, \Delta w \Delta h\right) = \prod_{k=1}^{n} \frac{\left(\exp\left(\tilde{f}_k\right)\Delta w \Delta h\right)\exp\left(\exp\left(\tilde{f}_k\right)\Delta w \Delta h\right)}{(\tilde{v}_k)!}. \quad (13)$$

Based on (6) and (1), $\hat{f}$ can be expressed as

$$\hat{f} = \arg\max_{\tilde{f}} \left[p\left(\tilde{f} \middle| \tilde{u}, \tilde{v}\right) \right] = \arg\max_{\tilde{f}} \left[\frac{p\left(\tilde{v} \middle| \tilde{f}\right) p\left(\tilde{f} \middle| \tilde{u}\right)}{\int p\left(\tilde{v} \middle| \tilde{f}\right) p\left(\tilde{f} \middle| \tilde{u}\right) df} \right]. \quad (14)$$

In order to simplify the calculation, logarithm of posterior probability

$$\hat{f} = \arg\max_{\tilde{f}} \left[\ln \left(\frac{p\left(\tilde{v} \middle| \tilde{f}\right) p\left(\tilde{f} \middle| \tilde{u}\right)}{\int p\left(\tilde{v} \middle| \tilde{f}\right) p\left(\tilde{f} \middle| \tilde{u}\right) df} \right) \right] = \arg\max_{\tilde{f}} \left[\ln p\left(\tilde{v} \middle| \tilde{f}\right) + \ln p\left(\tilde{f} \middle| \tilde{u}\right) \right]. \quad (15)$$

Based on the assumption of zero mean prior distribution of Gauss processes $f(u)$, which means $\tilde{f} \middle| \tilde{u} \sim N(0, C_{\tilde{u}\tilde{u}})$, the prior is

$$p\left(\tilde{f} \middle| \tilde{u}\right) = \frac{1}{(2\pi)^{\frac{n}{2}} |C_{\tilde{u}\tilde{u}}|} \exp\left(-\frac{1}{2} \tilde{f}^T C_{\tilde{u}\tilde{u}}^{-1} \tilde{f} \right). \quad (16)$$

Substituting (14) and (12) back to (13), $\hat{f}$ can be found by the Newton method [29]. Substituting $\hat{f}$ back to (7), the negative Hessian matrix Q can be solved. Furthermore, we can get the feature points' density by (10) and (15)

$$\begin{aligned} S &= C_{u^*u^*} - C_{u^*\tilde{u}} \left(C_{\tilde{u}\tilde{u}} + Q^{-1} \right)^{-1} C_{\tilde{u}u^*} \\ E &= \exp\left(C_{u^*\tilde{u}} C_{\tilde{u}\tilde{u}}^{-1} \hat{f} + \frac{1}{2} S \right) \\ D &= \exp\left(2 C_{u^*\tilde{u}} C_{\tilde{u}\tilde{u}}^{-1} \hat{f} + S \right) (\exp(S) - 1). \end{aligned} \quad (17)$$

C. Terrain Assessment Criteria Based on Feature Density

In this section, a feature density factor (E, D) based terrain assessment criteria is established by the feature density mean value and variance. To avoid the shortage of two-valued logic, here, we adopt fuzzy logic reasoning terrain safety. The fuzzy reasoning consists of a set of fuzzy rules in the form

$$\text{IF } A \text{ AND } B, \text{ THEN } C \quad (18)$$

where conditions A and B are composed of fuzzy input variables (e.g., feature density factor), action C is a fuzzy set of variables (e.g., terrain safety), AND is the fuzzy connective. Action C is evaluated based on the membership function of condition A and condition B. The input linguistic labels for the feature density mean value are $A = \{S_E, M_E, L_E\}$ and for the feature density variance are $B = \{S_D, M_D, L_D\}$, which stand for Small, Medium, and Large. The action linguistic labels for terrain safety are $C = \{P, L, M, H\}$, which stand for Poor, Low, Medium, and High. The input variables are normalized and the membership functions are bell functions

$$h(\alpha) = \frac{1}{1 + \left(\frac{\alpha - t}{r} \right)^{2s}} \quad (19)$$

where α stands for the fuzz variables and r, s, and t stand for the parameters that are different from different fuzzy variables. The fuzzy rules are connected by Fig. 6, for instance, the first rule is IF A is S_E AND B is S_D, THEN C is H.

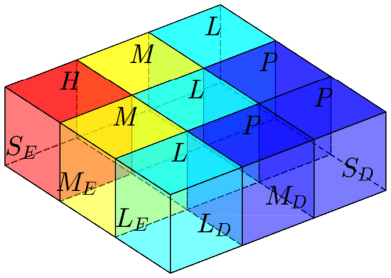

Fig. 6. Rules for terrain safety evaluation.

The safety score of landing terrain is obtained by the centroid defuzzification method. Terrain safety evaluation result $F(E, D)$ is combined by the degrees of membership to the fuzzy classes

$$F(E, D) = \frac{\sum_{i=1}^{4} m_i I_i}{\sum_{i=1}^{4} I_i} \quad (20)$$

where m_i is the peak value of the membership function based on the fuzzy rules, I_i is the area under the truncated membership function. Define J_s as the safety score at specific pixel position as follows:

$$J_s = \frac{F(E, D) - F_{\min}}{F_{\max} - F_{\min}} \quad (21)$$

where $F_{\max}$ and $F_{\min}$ are the maximum and minimum terrain safety evaluation value of the image.

IV. Applications on Multitypes Terrain Hazard Detection and Assessment

In this section, the method we presented above is tested by several planetary complex terrain images acquired from terrain simulations. The terrain images consist of discontinuities, craters, and mountains with complex shapes and locations. On this basis, in order to further verify the performance of the algorithm, the random terrain generation method for complex hazardous terrain were simulated, and the method of Monte Carlo is used to testify the performance of hazard detection.

A. Simulation Environments

In this paper, the simulated terrain is obtained by using the real terrain DEM from HiRISE [33] and simulated terrain superposition method, and the simulated terrain image is obtained by computer graphics methods during a descending process. In the simulation experiments, the safety requirements of the landing probe and simulation conditions for the landing scenes are shown in Table III. Fig. 7(a) is the simulated terrain's DEM. According to the landing safety requirements given in Table III, the safety of the landing area is assessed by combining the detections of craters and rocks. The least squares plane fitting is applied to the topographic map within the landing radius, and the angle

TABLE III
Standards of Safety Zone and Working Environments

Minimal safety landing radius	10m	Working height h	100m< h <500m
Safety slope angle	$< 15°$	Lighting conditions	The incident angle should not too low
Safety distance from rocks	> 4m	Landing attitude	Camera plane parallel with ground plane
Safety distance from craters	> 4m	Landing trajectory	Direct injection trajectory

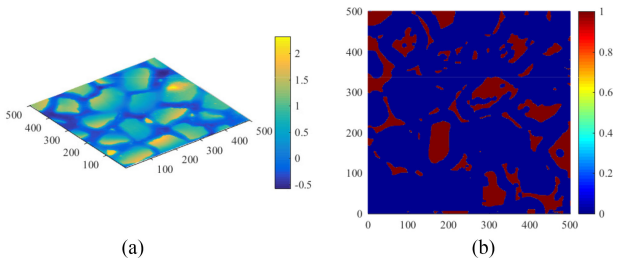

Fig. 7. Simulated terrain DEM and the safety truth map.

between the plane normal vector and the vertical coordinate axis of the landing coordinate system is recorded as the terrain slope angle. The terrain safety truth map is shown in Fig. 7(b)

In the following simulation experiments, the landing safety standards are the same as shown in Table III, which is also used to get the result of the landing terrain safety truth map. The accuracy of the algorithm is judged by the safety detect correct ratio$R_{\text{safe_right}}$, the safety detect error ratio $R_{\text{safe\_wrong}}$, the danger detect correct ratio $R_{\text{danger\_right}}$, and the danger detect error ratio $R_{\text{danger\_wrong}}$:

$$
\begin{aligned}
R_{\text{safe\_right}} &= \frac{S(A_{\text{detection\_safe}} \cap A_{\text{safe}})}{S(A_{\text{safe}})} \\
R_{\text{safe\_wrong}} &= \frac{S(A_{\text{detection\_safe}} \cap A_{\text{danger}})}{S(A_{\text{safe}})} \\
R_{\text{danger\_right}} &= \frac{S(A_{\text{detection\_danger}} \cap A_{\text{danger}})}{S(A_{\text{danger}})} \\
R_{\text{danger\_wrong}} &= \frac{S(A_{\text{detection\_danger}} \cap A_{\text{safe}})}{S(A_{\text{safe}})}
\end{aligned} \tag{22}
$$

where, A_{danger} represents the regions of reality hazard terrain. A_{safe} represents the regions of reality safety terrain, $A_{\text{detection\_safe}}$ and $A_{\text{detection\_danger}}$ represent, respectively, the regions of safe terrain and dangerous terrain detected by our algorithm. $\cap$ represents the overlapping regions, and $S(\cdot)$ represents the area of the regions.

B. Case 1-Gully Terrain

The plateau terrain is a typical discontinuous terrain hazard. Fig. 8(a) shows a simulated terrain image generated by Mars terrain DEM superimposed with a random terrain. Fig. 8(b) shows the terrain safety truth map. From the image shown in Fig. 8(a) and safety map shown in Fig. 8(b), we can conclude that the terrains A, B, and C have large and flat surface that can be used for landing. The simulated

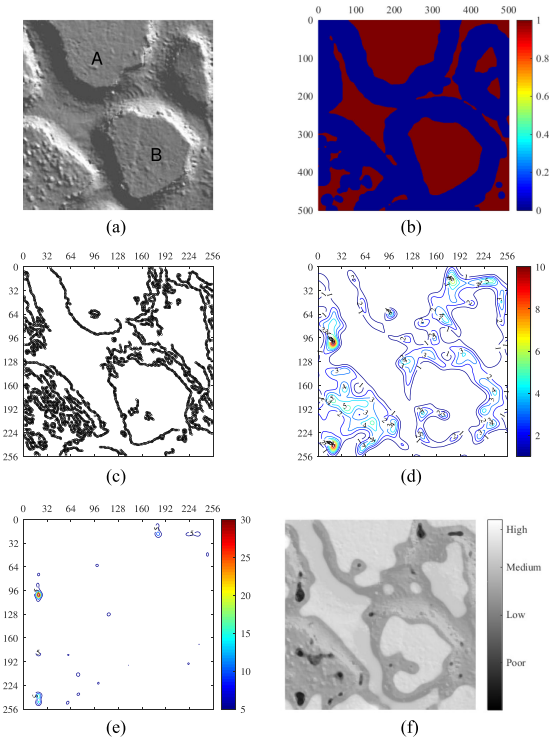

Fig. 8. Simulated gully terrain and detection results. (a) Simulated terrain image. (b) Safety truth map. (c) Feature points. (d) Mean of the density. (e) Covariance of density. (f) Detection results of the density-based method.

TABLE IV
Gully Terrain Detection Performance

Algorithm	Run time	safety detect correct ratio
Density based	1.480656s	0.582655
safety detect error ratio	danger detect correct ratio	danger detect error ratio
0.518703	0.647567	0.229069

terrain resolution is 0.1 m per pixel, shooting height is 400 m, and image resolution is 0.15 m per pixel. The gullies' width are around 10 m, which are dangerous to the probe. Fig. 8(c) shows the results of feature points extracted by sobel operator. Fig. 8(d) and (e) show the results of density mean and covariance, respectively. The safety results of the terrain detected by our algorithm is shown in Fig. 8(f), this results are superimposed with the terrain image. The performance of the algorithm is shown in Table IV. The safety detect correct ratio and the danger detect correct ratio are both 60%. Considering these terrain's hazard, the detection method needs to be determined artificially; hence, our algorithm could be suitable for these gully terrains and also as the predetection for traditional method in addition.

C. Case 2-Crater Terrain

The detection of special complex craters is still the difficulty of hazard detection, which mainly exists in overlapping craters and edge-blurred craters. For the overlapping and the edge-blurred craters,' shapes are difficult to be depicted accurately, increasing the complexity of hazard detection. Fig. 9(a) shows the image of overlapped crater,

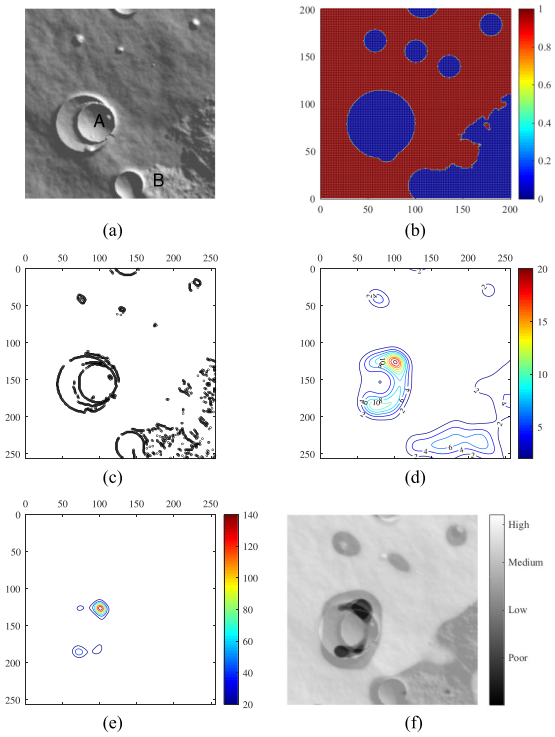

Fig. 9. Overlapped crater terrain and detection results. (a) Simulated terrain image. (b) Safety truth map. (c) Feature points. (d) Mean of the density. (e) Covariance of density. (f) Detection results of the density-based method.

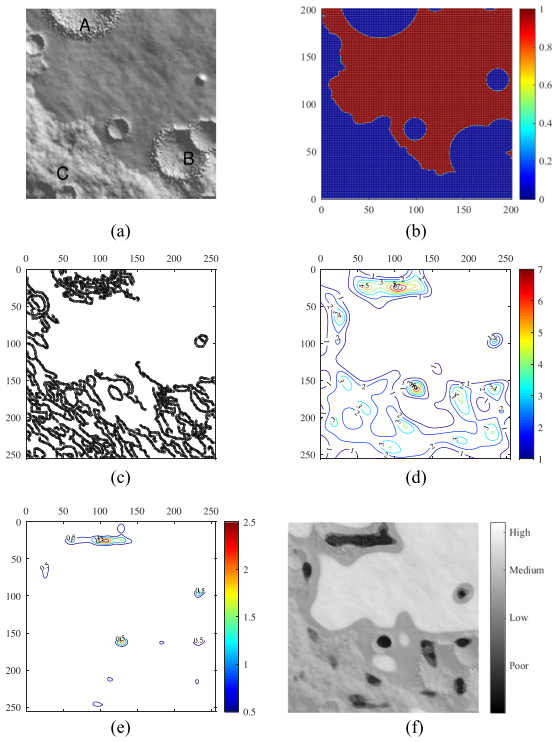

Fig. 10. Simulated edge-blurred terrain and detection results. (a) Simulated terrain image. (b) Safety truth map. (c) Feature points. (d) Mean of the density. (e) Covariance of density. (f) Detection results of the density-based method.

TABLE V
Overlapped Crater Terrain Detection Performance

Algorithm	Run time	safety detect correct ratio
Density based	0.377616s	0.873691
safety detect error ratio	danger detect correct ratio	danger detect error ratio
0.047905	0.834500	0.229069

TABLE VI
Edge-Blurred Terrain Detection Performance

Algorithm	Run time	safety detect correct ratio
Density based	0.812360s	0.669593
safety detect error ratio	danger detect correct ratio	danger detect error ratio
0.013774	0.990822	0.360959

and Fig. 9(b) shows the safety truth map. The simulated terrain resolution is 1.15 m per pixel, shooting height is 200 m, and image resolution is 0.78 m per pixel. Fig. 9(c) shows the results of feature points extracted by the sobel operator. Fig. 9(d) and (e) show the results of density mean and covariance, respectively. The safety results of the terrain detected by our algorithm is shown in Fig. 9(f). The performance of our algorithm is shown in Table V, the safety detect correct ratio and the danger detect correct ratio are both greater than 80%. Therefore, the hazard detection algorithm presented in this paper can effectively detect danger region caused by the overlapping craters.

The edge-blurred craters formed in early geological age. And then under the influence of geological movement and other natural corrosion, the edges of the craters are no longer clear, which makes the craters don't have the regular geometric shape. This is one of the difficulties of detection. Fig. 10(a) shows the image of edge-blurred craters and Fig. 10(b) shows the safety truth map. The simulated terrain resolution is 1.15 m per pixel, shooting height is 200 m, and the image resolution is 0.78 m per pixel. Fig. 10(c) shows the results of feature points extracted by the sobel operator. Fig. 10(d) and (e) show the results of density mean and covariance, respectively. The safety results of the terrain detected by our algorithm is shown in Fig. 10(f). The performance of our algorithm is shown in Table VI. The safety detect correct ratio is 67% and the danger detect correct ratio is 99%. The safety detect correct ratio performs in general, but the danger detect correct ratio is very high, this means that the algorithm detect most of the danger area. Even the overlapping safe region is small, but the hazardous area has been effectively detected.

D. Case Three-Mountain and Valley Terrain

Mountain and valley terrains are the main hazards threat to the lander's security. The mountain and the canyon images are similar in natural light, the main difference is the shadings direction. Fig. 11(a) shows the image of random simulation terrain and Fig. 11(b) shows the safety truth map. The simulated terrain resolution is 0.92 m per pixel, shooting height is 400 m, and the image resolution is 1.95 m per pixel. Fig. 11(c) shows the results of feature points extracted by the sobel operator. Fig. 11(d) and (e) show the results of density mean and covariance, respectively. The

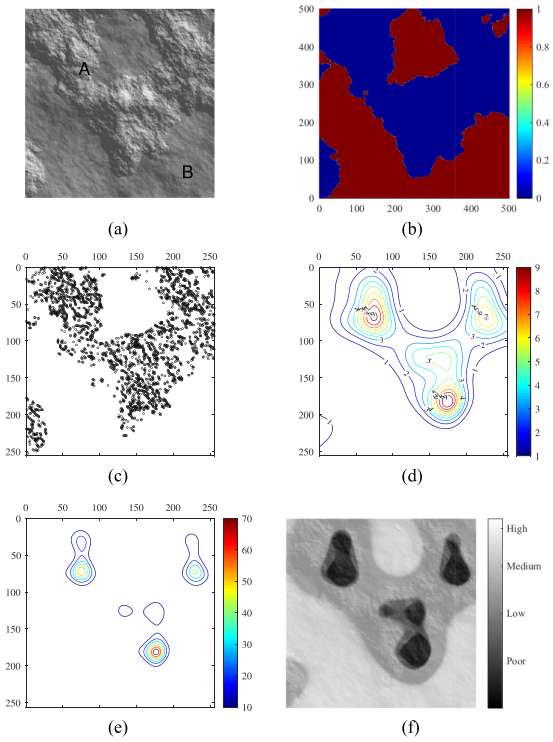

Fig. 11. Simulated mountain terrain and detection results. (a) Simulated terrain image. (b) Safety truth map. (c) Feature points. (d) Mean of the density. (e) Covariance of density. (f) Detection results of the density-based method.

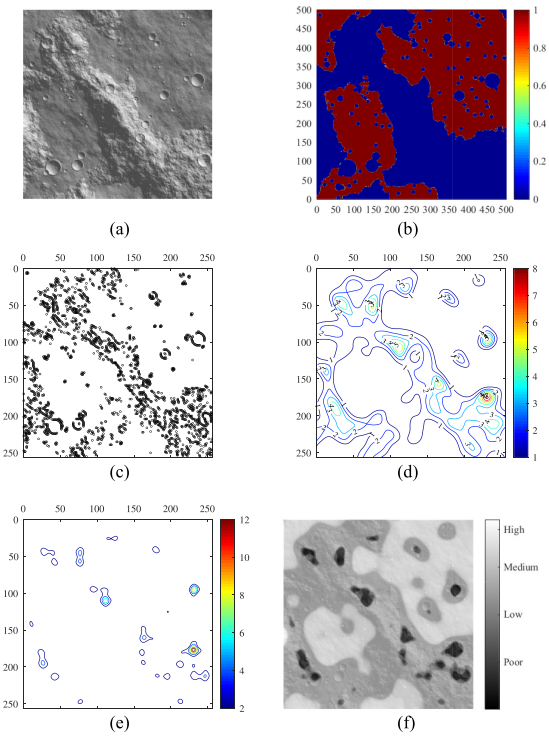

Fig. 12. Simulated multitypes hazard terrain and detection results. (a) Simulated terrain image. (b) Safety truth map. (c) Feature points. (d) Mean of the density. (e) Covariance of density. (f) Detection results of the density-based method.

TABLE VII
Mountain Terrain Detection Performance

Algorithm	Run time	safety detect correct ratio
Density based	0.176157s	0.751311
safety detect error ratio	danger detect correct ratio	danger detect error ratio
0.082521	0.866142	0.170231

TABLE VIII
Multitypes Hazard Terrain Detection Performance

Algorithm	Run time	safety detect correct ratio
Density based	1.063198s	0.566364
safety detect error ratio	danger detect correct ratio	danger detect error ratio
0.105694	0.894312	0.301974

safety results of the terrain detected by our algorithm is shown in Fig. 11(f). The performance of our algorithm is shown in Table VII. The safety detect correct ratio is greater than 75%, and the danger detect correct ratio is greater than 85%. Due to the high altitude, the detector can have enough time to maneuver.

E. Case Four-Multitypes Hazards Terrain

The detection of various complex terrain often uses a fusion of multitypes hazard detection methods, which is not suitable for low-power, small-cost detection mission's requirements. Therefore, there is a need for the hazard method capable of realizing the detection of multitypes hazard terrains under the requirements of low power and light weight. Fig. 12(a) shows the image of random simulation terrain and Fig. 12(b) shows the safety truth map. The simulated terrain resolution is 0.92 m per pixel, shooting height is 400 m, and the image resolution is 1.95 m per pixel. Fig. 12(c) shows the results of feature points extracted by the sobel operator. Fig. 12(d) and (e) show the results of density mean and covariance, respectively. The safety results of the terrain detected by our algorithm is shown in Fig. 12(f). The performance of our algorithm is shown in Table VIII. The safety detect correct ratio is 57% and the danger detect correct ratio is 89%, our methods can detect the hazardous in terrains with multitypes. In this paper, the hazard detection method is relatively conservative in the detection rate, that is, as far as possible to achieve the detection of dangerous areas, which will improve the probability of safe landing of the lander.

We use Monte Carlo based simulations to further evaluate the performance of the feature-based hazard detection method. The simulations use the simulated random terrain. One thousand landing terrains are generated in different craters, rocks, mountains, and illumination conditions. One hundred terrain images of the simulations are shown in Fig. 13; the simulations conditions are shown in Table IX. The size of terrain is 500 m $\times$ 500 m and the simulation conditions are the size of mountains, rocks, and craters. The images are generated at a height of 400 m, 60° of FOV, 50.00 mm of focal length, and resolution of 256 $\times$ 256 pixel.

Fig. 14 gives the performance of the hazard detection algorithm. The safety detect correct ratio are mostly higher

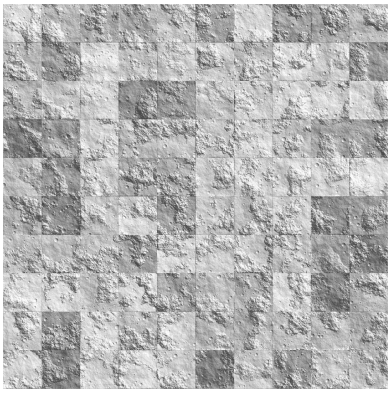

Fig. 13. One hundred random terrain image simulations.

TABLE IX
Terrain Simulation Conditions

Range of parameters	The ratio of hazard terrain to the whole terrain	The ratio of mountains to whole terrain
Mean value	0.4	0.5
fluctuation range	20%	15%
	Craters size (m)	Rocks size (m)
Mean value	40	5
fluctuation range	60%	20%

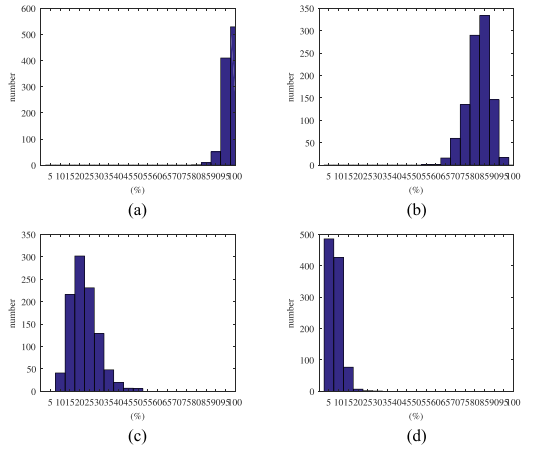

Fig. 14. Feature-density-based hazard detection and evaluation results of random terrains. (a) Safety detect correct ratio. (b) Danger detect correct ratio. (c) Safety detect error ratio. (d) Danger detect error ratio.

than 90%, 529 simulations are higher than 95%. The danger detect correct ratio are mostly higher than 75% with 992 simulations. The safety detect error ratio of 919 simulations are lower than 30%, and the danger detect error ratio of 913 are lower than 10%. These simulations show that the algorithm is stricter in danger detection, which means the algorithm should not identity the danger area to safety area. Feature density based hazard detection and evaluation method performs well in these simulations and get high identification rate from these results.

V. CONCLUSION

The concept of terrain feature density is introduced into the process of terrain hazard detection and assessment. An innovative method of terrain hazard detection and assessment is presented in this paper. Different from former methods, we focus on a unified representation method of terrain hazards instead of representations of specific types. We solve the problems of multitypes terrain hazards detection for low cost and small weight missions, which is not suitable for the traditional methods. Simulation and analysis results show that our method can handle discontinuous, complex shapes and blurred edges hazards in the harsh environment. For multitypes of complex hazards, our method also performs well. The simulations based on the Monte Carlo method show that the presented method have good adaptability of different terrain environment in 1000 simulation results. Besides, this method introduces Gaussian processes machine learning in feature density estimation, which improves the application potential of the onboard real-time system.

REFERENCES

[1] J. A. Grant, M. P. Golombek, T. J. Parker, J. A. Crisp, S. W. Squyres, and C. M. Weitz
Selecting landing sites for the 2003 mars exploration rovers
Planet. Space Sci., vol. 52, no. 1–3, pp. 11–21, 2004.

[2] L. M. Feetham, N. Aouf, C. Bourdarias, and T. Voirin
Single camera absolute motion based digital elevation mapping for a next generation planetary lander
Acta Astronautica, vol. 98, no. 5, pp. 169–188, 2014.

[3] E. C. Wong, G. Singh, and J. P. Masciarelli
Guidance and control design for hazard avoidance and safe landing on mars
J. Spacecraft Rockets, vol. 43, no. 2, pp. 378–384, 2006.

[4] A. E. Johnson, A. R. Klumpp, J. B. Collier, and A. A. Wolf
Lidar-based hazard avoidance for safe landing on mars
J. Guid. Control Dyn., vol. 25, no. 6, pp. 1091–1099, 2002.

[5] A. Huertas, Y. Cheng, and L. H. Matthies
Real-time hazard detection and avoidance demonstration for a planetary lander
In *Proc. AIAA SPACE 2014 Conf. Expo.*, 2014, pp. 24–46.

[6] J. A. Keim *et al.*
Field test implementation to evaluate a flash lidar as a primary sensor for safe lunar landing
In *Proc. Aerosp. Conf.*, 2010, pp. 1–14.

[7] X. Xiao, H. Cui, and Y. Tian
Robust plane fitting algorithm for landing hazard detection
IEEE Trans. Aerosp. Electron. Syst., vol. 51, no. 4, pp. 2864–2875, Oct. 2015.

[8] Y. Cheng, A. E. Johnson, L. H. Mattheis, and A. A. Wolf
Passive imaging based hazard avoidance for spacecraft safe landing
In *Proc. 6th Int. Symp. Artif. Intell., Robot. Autom. Space*, 2001, pp. 1–8.

[9] K. Matsumoto *et al.*
Optical sensors in obstacle detection and avoidance for moon landing
In *Proc. 7th Int. Symp. Artif. Intell., Robot. Autom. Space*, 2003, pp. 638–647.

[10] T. Brady, E. Robertson, C. Epp, S. Paschall, and D. Zimpfer
Hazard detection methods for lunar landing
In *Proc. 2009 IEEE Aerosp. Conf.*, Mar. 2009, pp. 1–8.

[11] L. Matthies, A. Huertas, Y. Cheng, and A. Johnson
Stereo vision and shadow analysis for landing hazard detection
In *Proc. IEEE Int. Conf. Robot. Autom.*, 2008, pp. 2735–2742.

[12] S. Woicke and E. Mooij
A stereo-vision hazard-detection algorithm to increase planetary lander autonomy
Acta Astronautica, vol. 122, no. 4, pp. 42–62, 2016.

[13] M. Bajracharya
Single image based hazard detection for a planetary lander
In *Proc. 5th Biannu. Autom. Congr.*, 2002, pp. 585–590.

[14] A. Huertas, Y. Cheng, and R. Madison
Passive imaging based multi-cue hazard detection for spacecraft safe landing
In *Proc. IEEE Aerosp. Conf.*, 2006, pp. 14–27.

[15] B. Leroy, G. Medioni, E. Johnson, and L. Matthies
Crater detection for autonomous landing on asteroids
Image Vis. Comput., vol. 19, no. 11, pp. 787–792, 2001.

[16] T. Barata, E. I. Alves, J. Saraiva, and P. Pina
Automatic recognition of impact craters on the surface of mars
In *Proc. Int. Conf. Image Anal. Recognit.*, 2004, vol. 3212, no. 3212, pp. 489–496.

[17] R. Martins, P. Pina, J. S. Marques, and M. Silveira
Crater detection by a boosting approach
IEEE Geosci. Remote Sens. Lett., vol. 6, no. 1, pp. 127–131, Jan. 2009.

[18] G. Salamuniccar and S. Loncaric
Method for crater detection from Martian digital topography data using gradient value/orientation, morphometry, vote analysis, slip tuning, and calibration
IEEE Trans. Geosci. Remote Sens., vol. 48, no. 5, pp. 2317–2329, May 2010.

[19] A. E. Johnson, Y. Cheng, and L. H. Matthies
Machine vision for autonomous small body navigation
In *Proc. Aerosp. Conf. Proc.*, vol. 7, 2000, pp. 661–671.

[20] F. Cmara *et al.*
Data fusion strategies for hazard detection and safe site selection for planetary and small body landings
CEAS Space J., vol. 7, no. 2, pp. 1–20, 2015.

[21] H. Seraji and N. Serrano
A multisensor decision fusion system for terrain safety assessment
IEEE Trans. Robot., vol. 25, no. 1, pp. 99–108, Feb. 2009.

[22] A. Discant, A. Rogozan, C. Rusu, and A. Bensrhair
Sensors for obstacle detection—A survey
In *Proc. Int. Spring Seminar Electron. Technol.*, 2007, pp. 100–105.

[23] A. M. Howard, B. M. Jones, and N. Serrano
Integrated sensing for entry, descent, and landing of a robotic spacecraft
IEEE Trans. Aerosp. Electron. Syst., vol. 47, no. 1, pp. 295–304, Jan. 2011.

[24] D. G. Krige
A statistical approach to some basic mine valuation problems on the witwatersrand
OR, vol. 4, no. 1, pp. 18–18, 1953.

[25] X. Liu, Q. Zhu, and H. Lu
Modeling multiresponse surfaces for airfoil design with multiple-output-Gaussian-process regression
J. Aircraft, vol. 51, no. 3, pp. 740–747, 2014.

[26] R. Dufour J. Muelenaere, and A. Elham
Trajectory Driven Multidisciplinary Design Optimization of a Sub-Orbital Spaceplane Using Non-Stationary Gaussian Process. New York, NY, USA: Springer-Verlag, 2015.

[27] H. Shang and Y. Liu
Assessing accessibility of main-belt asteroids based on Gaussian process regression
J. Guid. Control Dyn., vol. 40, no. 5, pp. 1–11, 2017.

[28] M. K. Titsias and N. D. Lawrence
Bayesian Gaussian process latent variable model
In *Proc. 13th Int. Workshop Artif. Intell. Statist.*, 2010, vol. 9, no. 9, pp. 844–851.

[29] C. K. I. Williams and D. Barber
Bayesian classification with Gaussian processes
IEEE Trans. Pattern Anal. Mach. Intell., vol. PAMI-20, no. 12, pp. 1342–1351, Dec. 1998.

[30] M. Seeger
Gaussian Processes for Machine Learning. Cambridge, MA, USA: MIT Press, 2006.

[31] J. F. C. Kingman
Poisson Processes. Hoboken, NJ, USA: Wiley, 2005.

[32] J. Moller, A. R. Syversveen, and R. P. Waagepetersen
Log Gaussian Cox processes
Scand. J. Statist., vol. 25, no. 3, pp. 451–482, 1998.

[33] A. S. Mcewen *et al.*
The high resolution imaging science experiment (HiRISE) during MRO's primary science phase (PSP)
Icarus, vol. 205, no. 1, pp. 2–37, 2010.

Ai Gao received the Ph.D. degree in aeronautical and astronautical science and technology from the Harbin Institute of Technology, Harbin, China, in 2012.

She is an Associate Professor with the School of Aerospace Engineering, Beijing Institute of Technology, Beijing, China. Her primary research focus is on the development of intelligent autonomous navigation and guidance method for spacecraft. Her research interests include autonomous navigation and control of spacecraft, image processing and hazard detection, trajectory design and guidance for planetary landing.

Shibo Zhou was born in 1992. He received the B.S. and M.S. degrees from the Beijing Institute of Technology, Beijing, China, in 2014 and 2017, respectively. His main research interests include image processing, machine learning, and vision-based navigation.